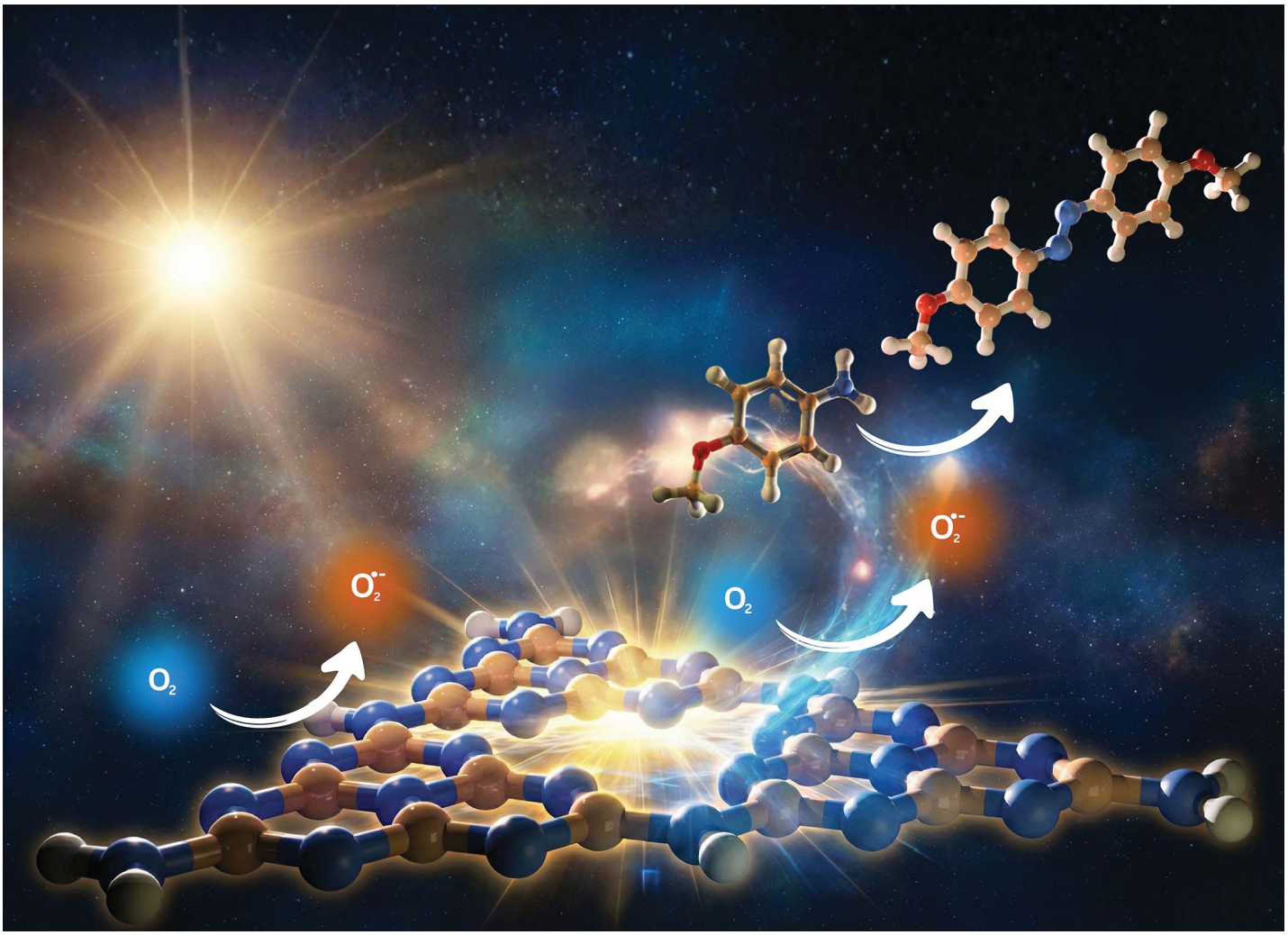

Highlighting research from Prof. Manoj B. Gawande's laboratory, Department of Industrial and Engineering Chemistry, Institute of Chemical Technology, Mumbai-Marathwada Campus, Jalna, India.

Harnessing an mpg-C_3N_4 photocatalyst for the selective oxidative coupling of amines to yield azoaromatic compounds

A sustainable, metal-free mpg-C_3N_4 photocatalyst drives the light-enabled oxidative coupling of aromatic amines using ambient air. Featuring a mesoporous architecture and efficient charge separation, the system achieves up to 99% conversion and selectivity with excellent recyclability. Mechanistic insights reveal superoxide radical-mediated pathways, offering a green and scalable route to azoaromatics.

Image reproduced by permission of Manoj B. Gawande from *J. Mater. Chem. A,* 2026, **14**, 14908.

Artwork partially generated using AI.

As featured in:

See Manoj B. Gawande *et al.*, *J. Mater. Chem. A,* 2026, **14**, 14908.

ROYAL SOCIETY OF CHEMISTRY

rsc.li/materials-a

Registered charity number: 207890

Journal of Materials Chemistry A

ROYAL SOCIETY OF CHEMISTRY

PAPER

View Article Online
View Journal | View Issue

Cite this: J. Mater. Chem. A, 2026, 14, 14908

Harnessing an mpg-C_3N_4 photocatalyst for the selective oxidative coupling of amines to yield azoaromatic compounds

Dinesh S. Chaudhari,[a] Rahul P. Gaikwad,[a] Indrajeet R. Warkad,[a] Rostislav Langer,[b] Michal Otyepka[bc] and Manoj B. Gawande[*ad]

Developing sustainable and efficient methods for the oxidative coupling of arylamines to generate aromatic azo compounds under mild conditions remains a significant challenge in the realm of sustainable chemistry. In this study, a metal-free mesoporous graphitic carbon nitride (mpg-C_3N_4) photocatalyst was synthesized *via* a straightforward one-step thermal polymerization reaction of urea, resulting in a high surface area of 109.40 m^2 g^{-1} and enhanced charge separation. The mpg-C_3N_4 photocatalyst was thoroughly characterized through XRD, XPS, HR-TEM, and BET analyses, confirming its mesoporous structure, crystallinity, and thermal stability. Under light irradiation in ambient air, mpg-C_3N_4 efficiently activated atmospheric O_2 to generate reactive superoxide radicals, enabling selective azo formation with up to 99% conversion and selectivity across a range of aromatic amines. DFT calculations and adsorption studies revealed the role of π–π stacking and favorable adsorption Gibbs energies, underpinning effective substrate activation and surface interaction. Mechanistic investigations, aided by EPR and DFT studies, elucidated that photoexcited electrons reduced O_2 to superoxide radicals, which mediated the oxidative coupling process. Reusability tests confirmed the catalyst's stability across five cycles, exhibiting no significant loss of activity or structural integrity. This sustainable, metal-free photocatalytic strategy, harnessing renewable light energy, not only demonstrates the scalable synthesis of azo compounds but also paves the way for new approaches to the green synthesis of functional azoaromatics.

Received 5th November 2025
Accepted 5th January 2026

DOI: 10.1039/d5ta08970k

rsc.li/materials-a

1 Introduction

The increasing global population and rapid industrialization have caused substantial environmental problems, such as the exhaustion of resources, increased pollution, and global warming.[1] As the demand for energy and chemical products continues to rise, traditional synthetic methods that often rely on non-renewable resources and generate hazardous wastes are exacerbating these issues.[2,3] Consequently, there is an urgent need for sustainable and efficient chemical processes that minimize environmental impacts while meeting the growing demands of society. In a time marked by increasing environmental challenges and the continuous quest for sustainable alternatives, photocatalysis has emerged as a transformative approach to address these issues by utilizing solar energy to drive chemical reactions under mild conditions. This technology decreases the reliance on fossil fuels while promoting the adoption of renewable resources, aligning with the principles of green chemistry.[4–9]

Photocatalysis, known for being both eco-friendly and energy-efficient, has emerged as a beacon of hope. This process is facilitated by suitable semiconductor photocatalysts that harness and utilize solar energy.[10] Numerous semiconductor photocatalysts, including graphitic carbon nitride (g-C_3N_4), zinc oxide, titanium dioxide, tungsten trioxide, tin oxide, cadmium sulfide, zinc sulfide, copper oxide, and lead sulfide, are used as supports and catalysts for several important advanced chemical transformations and sustainable applications.[11–15] Among these, g-C_3N_4 has garnered significant interest in the field of catalysis as it is a metal-free semiconductor with an ideal band gap of 2.7 eV, which allows for the efficient absorption of visible light.[16–18] Additionally, the synthesis of g-C_3N_4 from readily available starting materials like urea, melamine, thiourea, and cyanamide makes it not only cost-effective but also easy to produce.[3] As illustrated in Fig. 1a, it also allows for the straightforward tuning of its properties through synthetic modifications. Additionally, it is low in toxicity, has a suitable

[a]Department of Industrial and Engineering Chemistry, Institute of Chemical Technology, Mumbai, Marathwada Campus, Jalna 431213, Maharashtra, India. E-mail: mb.gawande@marj.ictmumbai.edu.in; mbgawande@gmail.com
[b]IT4Innovations, VSB – Technical University of Ostrava, 17. Listopadu 2172/15, 708 00 Ostrava-Poruba, Czech Republic
[c]Regional Centre of Advanced Technologies and Materials, The Czech Advanced Technology and Research Institute (CATRIN), Palacký University Olomouc, Šlechtitelů 27, 779 00 Olomouc, Czech Republic
[d]Nanotechnology Centre, Centre for Energy and Environmental Technologies, VŠB – Technical University of Ostrava, 17. Listopadu 2172/15, 708 00 Ostrava-Poruba, Czech Republic

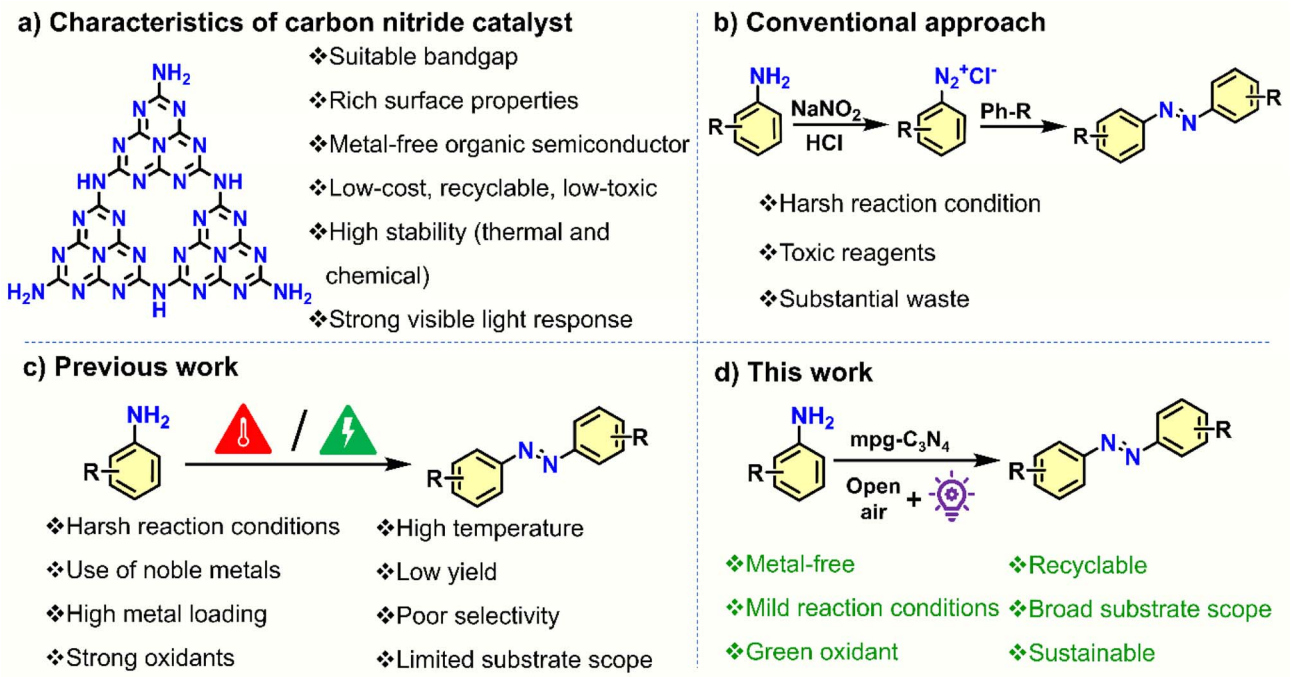

Fig. 1 (a) Characteristics of carbon nitride catalysts. (b) Scheme depicting a conventional approach for the synthesis of azoaromatics. (c) Previous literature reports on the synthesis of azoaromatics. (d) Our approach for the synthesis of azoaromatics.

band gap, demonstrates exceptional chemical stability even when exposed to reactive species, and has abundant surface properties that endow it with catalytic performance similar to that of homogeneous photocatalysts.[19–21] Since its first application as a metal-free photocatalyst for hydrogen generation by Wang *et al.*[22] in 2009, it has been extensively explored for various photocatalytic processes including CO_2 reduction, H_2O_2 production, organic transformations, and biomass valorization.[19,23–25] However, despite the unique electronic and mechanical properties of g-C_3N_4, its non-porous nature and relatively low surface area (<10 m^2 g^{-1}) limit its effectiveness in applications that require significant surface area and pore volume.[26] To overcome these limitations, the introduction of porosity into the carbon nitride matrix while preserving its inherent carbon and nitrogen chemistry offers a promising strategy for enhancing its performance in catalysis and adsorption.[26]

Aromatic azo compounds are important chemicals with diverse applications across pharmaceuticals, dyes, optical data storage, molecular switches, and numerous other industries.[27–31] In the textile industry, these compounds are used as dyes for fabric coloration.[32] Furthermore, the light-driven *trans–cis* isomerization of the N=N double bond in azo compounds leads to significant alterations in their physical properties. This transformation renders them particularly valuable for chemists in the development of protein probes, chemosensors, smart surface materials, and more.[33–35] Traditional methods for synthesizing azoaromatics often require harsh reaction conditions and toxic reagents and generate substantial wastes, posing environmental and economic challenges (Fig. 1b).[36] As the awareness of green chemistry increases, alternative sustainable synthetic methods are being investigated. These methods include the reductive coupling of nitrobenzenes, oxidative coupling of anilines, and oxidative dehydrogenation of hydrazobenzenes, all utilizing suitable catalytic systems to eliminate the use of hazardous diazonium intermediates.[37–39] Of all these methods, the oxidative coupling of readily accessible anilines using atmospheric air is particularly appealing. To date, all known catalytic systems (homogeneous/heterogeneous) for the direct oxidation of anilines rely on metals and perform efficiently under thermal and photocatalytic conditions (Fig. 1c).[28,40–48] Although efficient homogeneous and catalyst-free photocatalytic routes to azoaromatics have been reported, recyclable metal-free heterogeneous systems are still scarce.[49,50] Notably, the photochemical conversion of arylamines to azoaromatics has recently demonstrated moderate to good yields when utilizing an Ir-based photocatalyst.[27] While various catalysts, including noble metals, have been effectively investigated for the oxidative coupling of arylamines, significant challenges remain, like the need for high catalyst loading, stoichiometric reagents, strong oxidants, moderate yields, and a limited range of applicable substrates.[27,28,40–42,44,51,52] Therefore, the development of metal-free, sustainable, efficient, and selective catalysts for the transformation of amines to azoaromatics is of paramount importance.

Inspired by previous research, we developed a metal-free mesoporous carbon nitride (mpg-C_3N_4) photocatalyst for the oxidative coupling of arylamines to generate aromatic azo compounds under mild conditions (Fig. 1d). The mpg-C_3N_4 photocatalyst was produced *via* a straightforward one-step thermal polymerization reaction of urea, resulting in a higher

surface area of 109.40 m^2 g^{-1} and improved charge carrier transfer and separation compared to bulk g-C_3N_4. We explored the versatility of the mpg-C_3N_4 photocatalyst with various amine substrates, achieving conversion and selectivity up to 99% for the desired azoaromatics. This state-of-the-art mpg-C_3N_4 was compared with existing thermal catalysts and available photocatalysts for the oxidative coupling of amines. Mechanistic investigations supported by EPR and DFT studies demonstrated that the mpg-C_3N_4 photocatalyst can efficiently activate atmospheric O_2 molecules to produce superoxide radical anions ($O_2^{\bullet-}$), which are highly reactive oxygen species. Importantly, this catalyst can be easily separated from the reaction medium and reused by simple centrifugation, highlighting its potential as an effective heterogeneous photocatalyst. We anticipate that this research expands the range of applications, especially in the sustainable production of value-added chemicals and fuels, thus contributing significantly to advancements in the field.

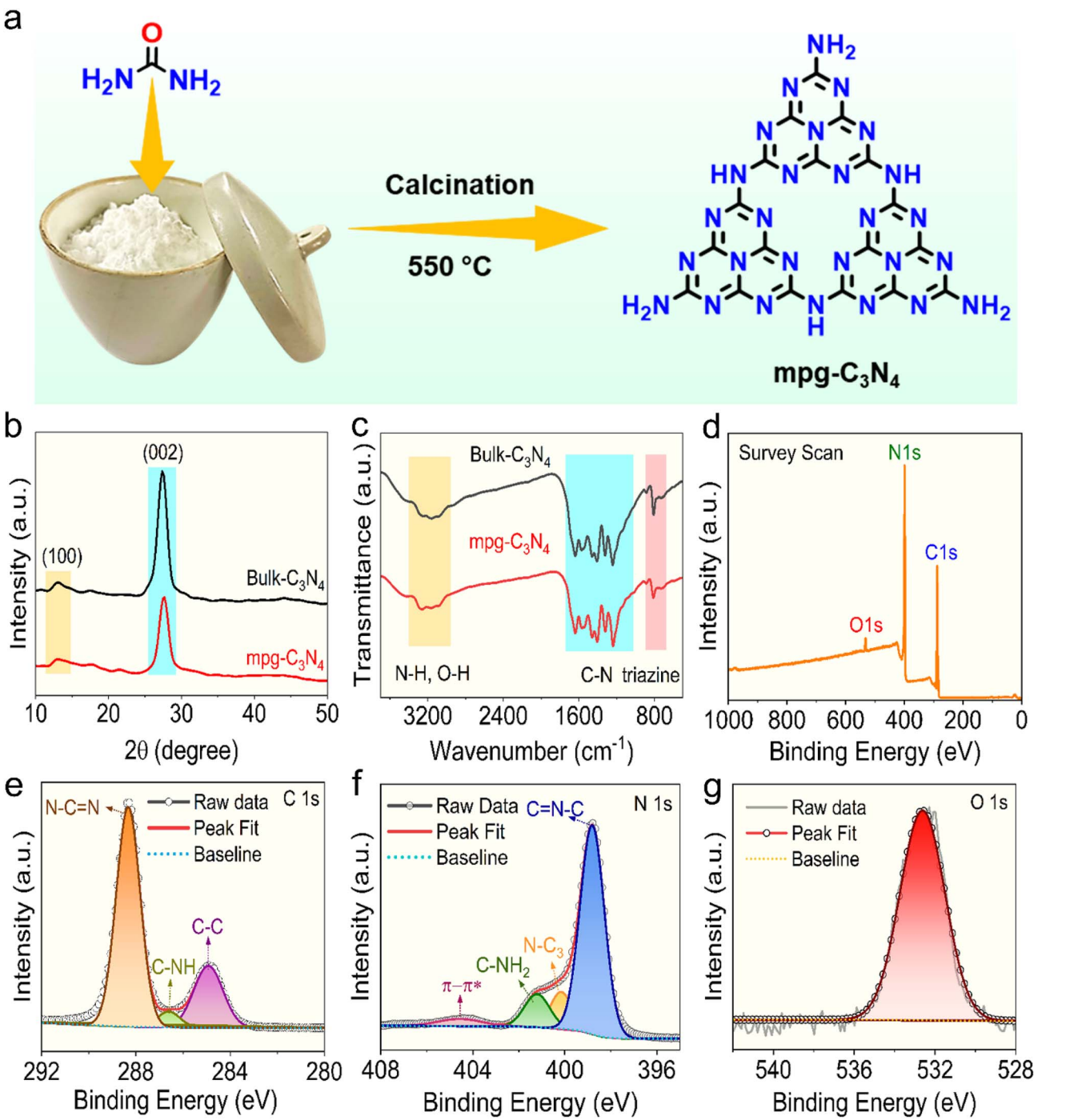

Fig. 2 (a) Scheme illustrating the synthesis of mpg-C_3N_4. (b) XRD patterns of mpg-C_3N_4 and bulk-C_3N_4. (c) FT-IR spectra of mpg-C_3N_4 and bulk-C_3N_4. (d) XPS survey scan, (e) C 1s, (f) N 1s, and (g) O 1s spectra of mpg-C_3N_4.

2 Results and discussion

2.1 Synthesis and characterization of catalysts

Mesoporous carbon nitride (mpg-C_3N_4) was synthesized using a one-step thermal polymerization method[13] (Fig. 2a); the detailed procedure is outlined in the experimental section of the SI. For the synthesis of mpg-C_3N_4, urea was placed in a porcelain crucible and calcined in a muffle furnace at 550 °C. Bulk carbon nitride (bulk-C_3N_4) derived from melamine was also produced using the same approach to compare photocatalytic performance.

Initially, powder X-ray diffraction (XRD) was used to examine the crystalline structure of mpg-C_3N_4 and bulk-C_3N_4 (Fig. 2b). The diffraction patterns of mpg-C_3N_4 and bulk-C_3N_4 displayed weak and strong peaks at 13.2° and 27.4°, respectively. The peak at 13.2° corresponds to the (100) plane and arises from the in-plane arrangement of tri-*s*-triazine motifs. Notably, the prominent peak at 27.4°, stemming from the (002) plane, is related to the stacking interactions between aromatic layers.[53] Structural features and chemical bonding types in the samples were further characterized using Fourier transform infrared (FT-IR) spectroscopy, with similar spectral profiles observed for mpg-C_3N_4 and bulk-C_3N_4, indicating comparable structural components (Fig. 2c). Both spectra show broad absorption peaks around 3000 cm^{-1} to 3400 cm^{-1} ascribed to the N–H and O–H stretching vibrations.[54] Additionally, a peak between 1150 cm^{-1} and 1750 cm^{-1} corresponds to the vibrational modes of the C–N heterocyclic groups, while sharp peaks at 810 and 890 cm^{-1} are attributed to the breathing mode of the tri-*s*-triazine units and N–H deformation mode.[55]

The XPS survey scan of mpg-C_3N_4 shows three peaks corresponding to C 1s, N 1s, and O 1s (Fig. 2d). The C 1s spectrum can be resolved into three distinct peaks with binding energies of 284.9, 286.6, and 288.3 eV (Fig. 2e). The peak at 284.9 eV is attributed to adventitious carbon (C–C), while the peaks at 286.6 eV and 288.3 eV correspond to C–NH_x (sp^2 hybridized carbon) and N–C=N within the tri-*s*-triazine structure of mpg-C_3N_4, respectively.[55,56] The N 1s spectrum was resolved into four peaks, with a dominant peak at 398.8 eV, indicating nitrogen atoms in an sp^2-hybridized state bonded to carbon. Additional peaks at 400.1 eV and 401.2 eV were ascribed to the tertiary N–C_3 and –NH_x functional groups associated with the tri-*s*-triazine backbone, respectively, while a minor peak at 404.5 eV was linked to π–π* excitation (Fig. 2f).[57] The O 1s spectrum reveals a peak at 532.2 eV, corresponding to the surface-bound moisture (Fig. 2g).[58,59]

To examine the surface structure of prepared mpg-C_3N_4, scanning electron microscopic (SEM) and high-resolution transmission electron microscopic (HR-TEM) analyses were performed. The SEM images displayed a loosely interconnected structure with visible gaps and void regions, indicating a porous and non-compact morphology (Fig. S1). The HR-TEM images of the mpg-C_3N_4 photocatalyst are illustrated in Fig. 3. The images reveal the nanowire-like morphology of mpg-C_3N_4 (Fig. 3a–c), indicating an irregular shape. This morphology can be correlated with the decomposition behaviour of the precursor, as the nature of the starting material strongly influences structural evolution during polymerization.[60,61] During the thermal breakdown of urea, gaseous species such as NH_3 and CO_2 are released, and these evolving gases act as *in situ* soft templates that promote the modification of the textural properties of the material.[62,63] This process not only influences the morphology but also leads to the formation of pores within the carbon nitride framework during polymerization. Earlier studies have shown that the evolution of gases within g-C_3N_4 domains can lead to the formation of internal pores, which can directly result in the development of mesoporosity and an increased specific surface area.[59,61] A similar phenomenon was observed in the mpg-C_3N_4 sample, as indicated by its significantly enhanced surface area (Fig. 3g and Table S1). This unique nanowire morphology of mpg-C_3N_4 is expected to enhance its photocatalytic activity.[13,64,65] The amorphous nature of the mpg-C_3N_4 sample was further validated by the selected area electron diffraction (SAED) pattern shown in the inset of Fig. 3b, which displays diffraction rings for the (100) and (002) planes, aligning well with the XRD findings.[66] Furthermore, EDX analysis indicated the presence of carbon and nitrogen in the mpg-C_3N_4 material, and elemental mapping corroborated these results (Fig. 3d–f).

The N_2 adsorption–desorption isotherms along with the BJH pore-size distribution for both bulk and mpg-C_3N_4 photocatalysts are illustrated in Fig. 3g and S2. The specific surface area (SSA), pore size, and pore volume of the carbon nitride materials are detailed in Table S1. The isotherms displayed a type-IV hysteresis loop, consistent with mesoporosity and confirming mesopores in both bulk-C_3N_4 and mpg-C_3N_4 photocatalysts.[67] The mpg-C_3N_4 sample exhibited an SSA of 109.40 $m^2\ g^{-1}$, significantly higher than that of bulk-C_3N_4, which measured 20.64 $m^2\ g^{-1}$ (Fig. 3g). Previous studies have shown that samples produced from urea as a precursor tend to have a greater SSA and pore volume than those derived from melamine.[68–70] The BJH pore-size distribution of mpg-C_3N_4 indicates an average pore size of 28.17 nm. Additionally, mpg-C_3N_4 exhibits a larger pore volume of 0.8025 $cm^3\ g^{-1}$, in contrast to bulk-C_3N_4, which has a pore volume of 0.1554 $cm^3\ g^{-1}$ (Table S1). These results confirm that the synthesized mpg-C_3N_4 sample is indeed mesoporous in nature. The higher SSA and mesoporous structure of mpg-C_3N_4 may enhance the electron mobility, improve light reflection and scatter within the material, and provide more reactive sites for effective interaction with reactants.[71,72] The number of basic sites in mpg-C_3N_4 and bulk-C_3N_4 was evaluated using the CO_2 temperature-programmed desorption (TPD) (Fig. 3h). It is well established that surface basicity is essential for the chemical adsorption of amines and the formation of surface complexes.[73] Both mpg-C_3N_4 and bulk-C_3N_4 displayed broad peaks in the range of 60 to 250 °C, which are associated with the physisorption and chemisorption of CO_2.[74,75] The basic site density was determined to be 0.091 mmol g^{-1} for mpg-C_3N_4 and 0.078 mmol g^{-1} for bulk-C_3N_4. The CO_2-TPD results confirmed that mpg-C_3N_4 exhibited greater basicity, which was correlated with its higher reactivity in the photocatalytic oxidation of amines.

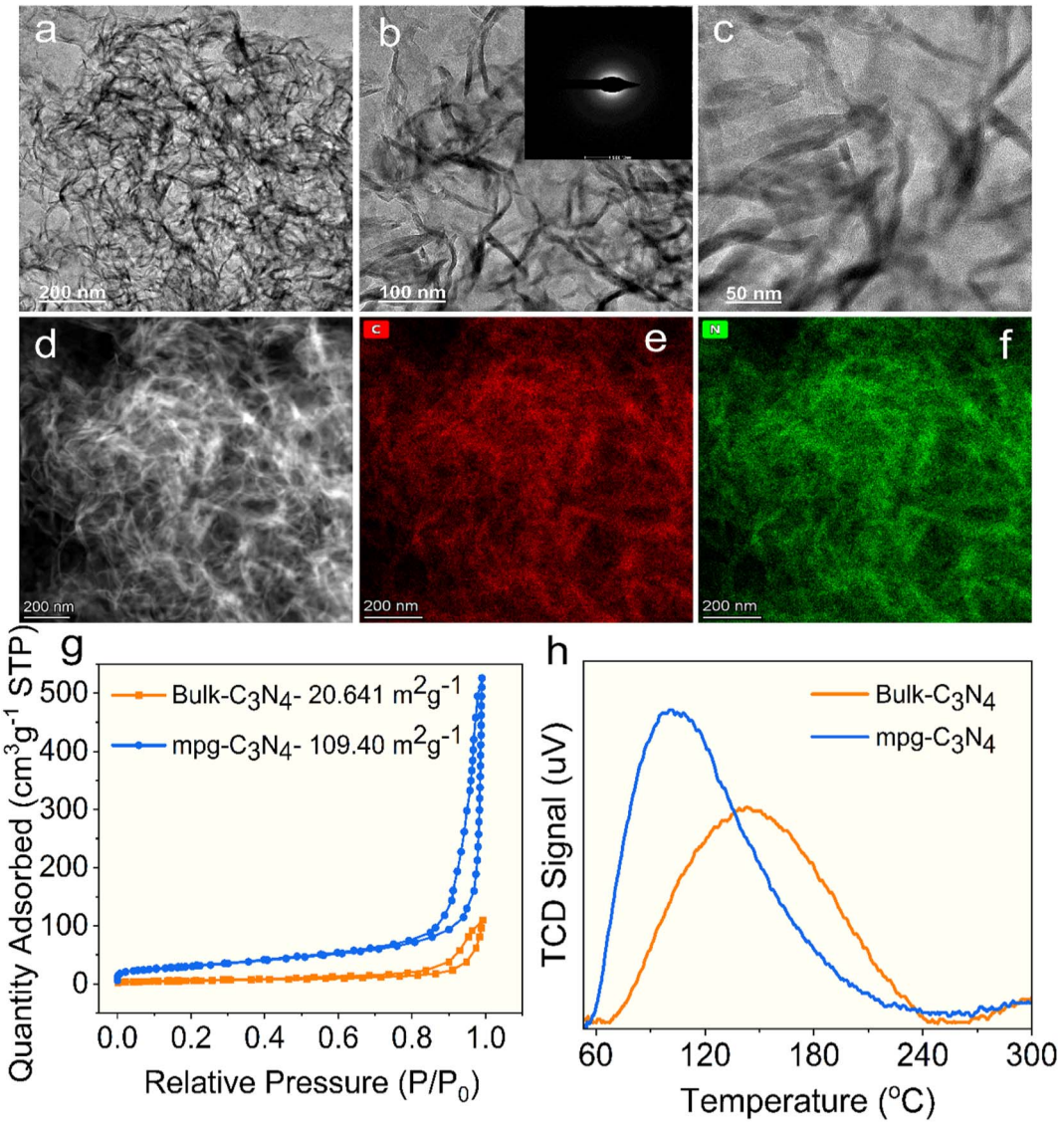

Fig. 3 (a–c) HR-TEM images of mpg-C_3N_4. (d) EDX analysis of mpg-C_3N_4. Elemental mapping of carbon (e) (red) and (f) nitrogen (green). (g) N_2 adsorption–desorption isotherm. (h) CO_2-TPD curves of mpg-C_3N_4 and bulk-C_3N_4.

The optical and electronic characteristics of bulk-C_3N_4 and mpg-C_3N_4 were examined to assess their photocatalytic performance. The obtained UV-vis diffuse reflectance spectra (DRS) are shown in Fig. 4a. The absorption band of mpg-C_3N_4 shows a blue shift compared to that of bulk-C_3N_4.[59] Using the Tauc plots, the bandgap energies were estimated to be approximately 2.70 eV for bulk-C_3N_4 and 2.94 eV for mpg-C_3N_4 (Fig. 4b). Furthermore, the charge separation and recombination dynamics of both materials were analyzed. The photoluminescence (PL) spectra of mpg-C_3N_4, excited at 385 nm, revealed that mpg-C_3N_4 displayed a lower PL intensity than that of bulk-C_3N_4 (Fig. 4c). The observed blue shift in the PL peak indicated a reduced recombination rate of photogenerated electron–hole pairs, which enhanced the photocatalytic performance of mpg-C_3N_4.[59,76,77]

To further investigate the transfer of photogenerated charge carriers, photo-electrochemical (PEC) studies were conducted. Electrochemical impedance spectroscopy (EIS) was performed to assess the electronic conductivity of the samples. The Nyquist plots showed that mpg-C_3N_4 exhibited a lower electronic resistance than that of bulk-C_3N_4, indicating reduced electron-transfer resistance (Fig. 4d). Additionally, linear sweep voltammetry (LSV) curves and transient photocurrent responses were recorded for both samples. Fig. 4e shows the current densities of bulk-C_3N_4 and mpg-C_3N_4 to be 0.063 mA cm^{-2} and 0.309 mA cm^{-2}, respectively, under dark conditions at 0 V *vs.* Ag/AgCl, indicating greater charge separation and transfer.[78,79] Fig. 4f compares the transient photocurrent responses of bulk-C_3N_4 and mpg-C_3N_4. Under light, photocurrents for both samples rise to their peak values and remain relatively stable. Upon switching off the light, the photocurrents return to baseline. Notably, mpg-C_3N_4 exhibits a higher photocurrent than that of bulk-C_3N_4, indicating its superior capability for separating and transferring photogenerated electron–hole pairs.[56] Overall,

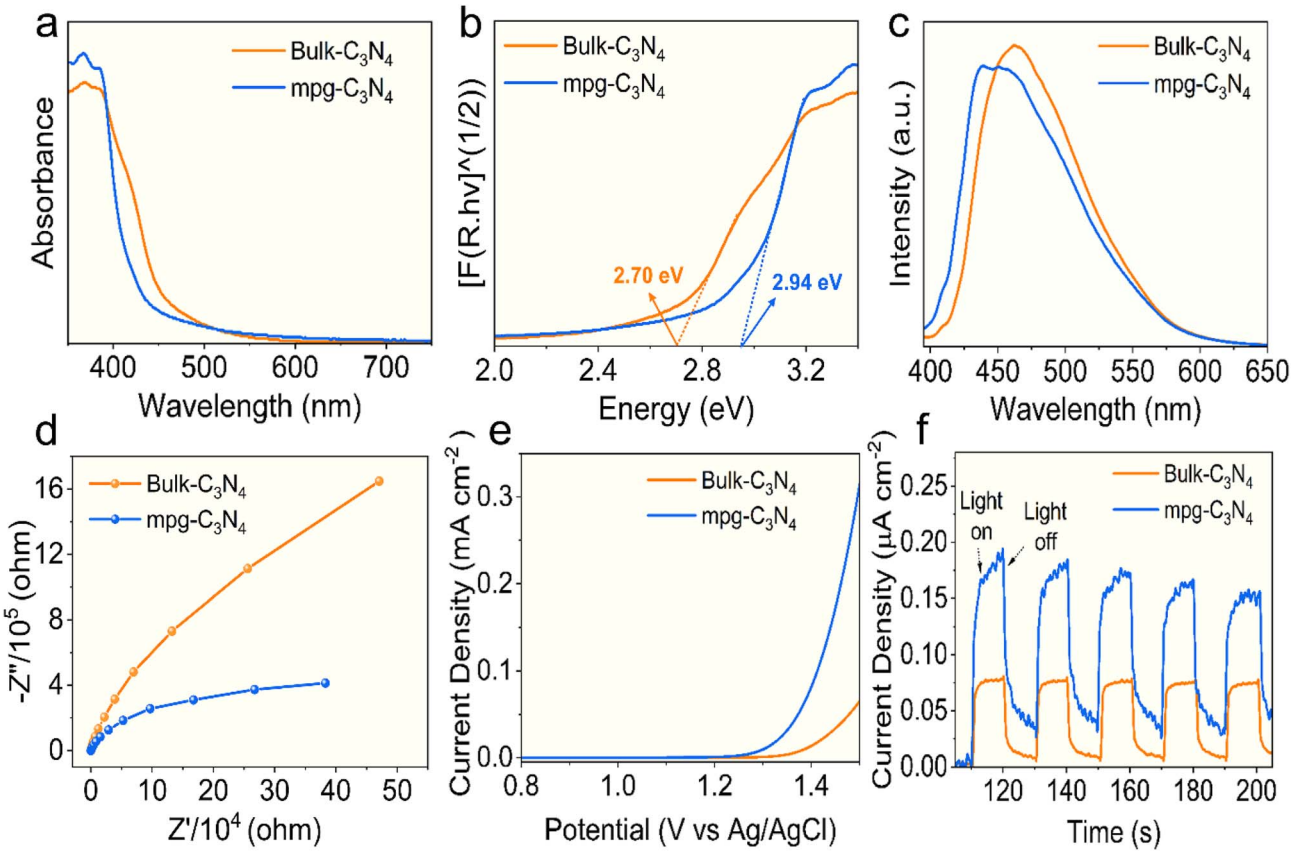

Fig. 4 (a) UV DRS spectrum, (b) bandgap, (c) PL spectra, (d) Nyquist plot, (e) LSV curves, and (f) transient photocurrent curves of mpg-C_3N_4 and bulk-C_3N_4.

these findings clearly demonstrate that mpg-C_3N_4 exhibits enhanced light absorption, charge transfer, and charge separation, implying enhanced photocatalytic efficiency.

2.2 Photocatalytic activity

Considering the remarkable physicochemical properties and the successful characterization of mpg-C_3N_4, it was further explored for the oxidative coupling of aryl amines to generate azoaromatics under light irradiation. A series of reactions was carried out to optimize this photocatalytic transformation, with the various conditions summarized in Table 1. The standard conditions were *p*-anisidine (0.1 mmol) as the substrate, 30 mg of the mpg-C_3N_4 photocatalyst, K_3PO_4 (1 equivalent) as a base, and 3 mL of DMSO as the solvent. In air, the reactions were performed under illumination at 395 nm (36 W lamp), at 30–35 °C for 24 h (detailed procedure is given in the SI). Under these standard conditions, the oxidative coupling of *p*-anisidine (**1a**) affords the corresponding azoaromatics (**2a**) with outstanding conversion (99%) and selectivity (98%) (Table 1, entry 1). The mpg-C_3N_4 sample shows a higher activity than that of bulk-C_3N_4 derived from melamine and under the same reaction conditions (Table 1, entry 2). The improved performance of mpg-C_3N_4 is due to its larger surface area (see Fig. 3g) and enhanced charge transfer dynamics (see Fig. 4d–f) compared to bulk-C_3N_4. Table 1 presents a series of control experiments, in which essential components are excluded from the reaction mixture, emphasizing the crucial roles of light and the catalyst (entries 3 and 4) in facilitating photoirradiation-driven oxidative coupling of amines. The effect of thermal heating was evaluated by carrying out the reaction at 55 °C without light (Table 1, entry 5), which resulted in no conversion of **1a**. Collectively, this finding underscores the significance of photocatalytic conditions. We also investigated the effect of light wavelength utilizing a 427 nm lamp (Table 1, entry 6), which afforded 47% conversion of **1a**. The influence of various solvents, including ACN, H_2O, and DMF as alternatives to DMSO was examined in the model reaction (Table 1, entries 7–9). ACN and H_2O exhibited relatively low conversions of **1a** (37% and 4%, respectively), while DMF achieved a higher conversion (78%), albeit with reduced selectivity toward **2a** (34%). In contrast, using DMSO afforded 98% conversion and 99% selectivity, likely due to the improved solubility of the reactants under light irradiation. The reaction requires a base (Table 1, entry 10) since proton removal is a key step in the photocatalytic oxidative coupling of amines.[49] Both inorganic base (KOAc) and organic base (NEt_3) were evaluated, resulting in 81% and 13% conversions of **1a**, respectively (Table 1, entries 11 and 12). Next, we investigated the effect of varying the K_3PO_4 concentration. Reducing the base to 0.5 equivalents decreased the conversion to 37%, indicating that an adequate concentration of base is essential for achieving optimal conversion (Table 1, entry 13).

Table 1 Optimization of reaction conditions[a]

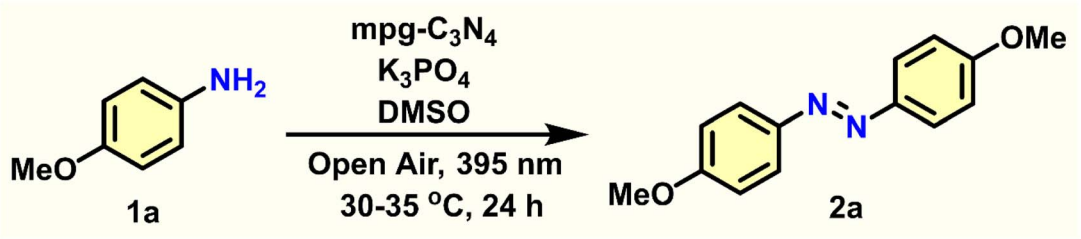

Entry	Deviation from standard conditions[a]	Conversion (**1a**)[b] (%)	Selectivity (**2a**)[b] (%)
1	None	99	98
2	Bulk-gC_3N_4	73	96
3	No light	N.D.[d]	N.D.
4	No catalyst	N.D.	N.D.
5	55 °C[c]	N.D.	N.D.
6	427 nm	47	98
7	ACN instead of DMSO	37	99
8	H_2O instead of DMSO	4	99
9	DMF instead of DMSO	78	34
10	No base	4	99
11	KOAc instead of K_3PO_4	81	96
12	NEt_3 instead of K_3PO_4	13	99
13	0.5 eq. of K_3PO_4	37	99
14	20 mg of mpg-C_3N_4	78	99

[a] Standard conditions: *p*-anisidine (0.1 mmol), mpg-C_3N_4 (30 mg), K_3PO_4 (1 eq.), DMSO (3 mL), air atmosphere, 395 nm lamp (36 W), 30–35 °C, 24 h. [b] Conversion and selectivity were determined by GC-MS analysis using dodecane as an internal standard. [c] Reaction performed at 55 °C without light irradiation. [d] N.D. = not detected.

Moreover, we assessed the effect of catalyst loading and observed a significant reduction in the conversion of **1a** to 79%, when the amount of mpg-C_3N_4 was decreased to 20 mg, highlighting the importance of maintaining an appropriate catalyst quantity (Table 1, entry 14).

With the optimal conditions established, mpg-C_3N_4 photocatalysts were used to synthesize aromatic azo compounds with a broad substrate scope from readily accessible primary amines, including those bearing electron-rich and electron-deficient groups (Table 2). Generally, amines with electron-rich characteristics (Table 2, entries **2a–2n**) exhibited significantly better conversion than those that were electron-deficient (Table 2, entries **2o–2x**). The influence of steric factors was also noted, as *para*-substituted anilines yielded higher conversion than their *ortho*-substituted counterparts (Table 2, entries **2b** and **2c**). Additionally, disubstituted aryl amines were effectively transformed into the corresponding azoaromatics, achieving good conversion rates (Table 2, entries **2e–2k**), although a slight decrease in product selectivity was observed for entries **2g** and **2k** due to the increased steric hindrance at the *ortho* position from the methyl ($-CH_3$) and isopropyl ($-C(CH_3)_2$) groups, respectively. Notably, the sterically hindered and electron-rich trimethyl aniline produced the azo derivative with a conversion and selectivity of 99% and 74%, respectively (Table 2, entry **2l**).

To further explore the behavior of aniline substrates during oxidative coupling in the presence of an amine group, a new substrate with an $-NH_2$ group at the *ortho* position of anilines was subjected to photocatalytic testing. The findings revealed that only one amine group was involved in forming the oxidative coupled product, achieving both conversion and selectivity of 99% (Table 2, entry **2m**). This selective coupling is attributed to steric hindrance from the additional $-NH_2$ groups, which restricts the reaction of the second amine after the first has coupled. An azoaromatic product with 70% conversion was also obtained from unsubstituted anilines (Table 2, entry **2n**). Importantly, halo-substituted anilines displayed good to moderate conversion, leading to the formation of halo-substituted azoaromatics (Table 2, entries **2o–2u**), which could be further utilized in transformations. The effect of steric hindrance in the case of halo-substituted anilines was also studied, as the conversion of *para*-substituted halides (Table 2, entries **2o–2r**) was significantly higher than that of the *ortho*-substituted halides (Table 2, entries **2s–2u**). Excellent conversions with good selectivity were also achieved with arylamines containing both electron-rich and electron-deficient groups (Table 2, entries **2v–2w**). In contrast, *p*-nitroaniline fails to produce any products, probably due to the significant electron deficiency of its amine group (Table 2, entry **2x**).

These findings indicate that mpg-C_3N_4 photocatalysts possess a significant tolerance to a variety of functional groups. Substrates with electron-rich groups (such as *para*-, *meta*-, and *ortho*-substituted variants) as well as those with electron-deficient groups were effectively converted, achieving

Table 2 Substrate scope for the photocatalytic oxidative coupling of arylamines to synthesize aromatic azo compounds using optimized conditions[a]

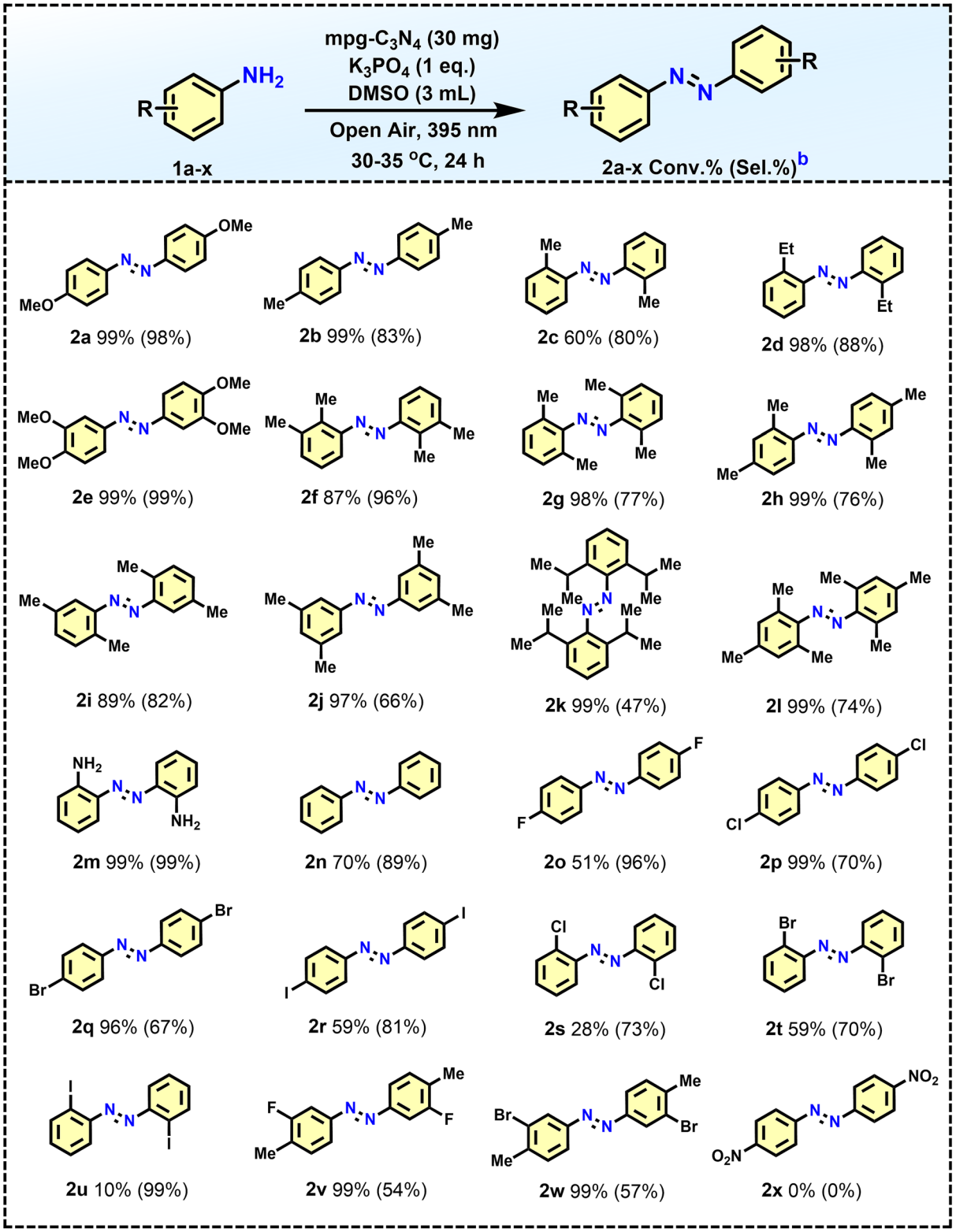

[a] Reaction conditions: amine (0.1 mmol), mpg-C_3N_4 (30 mg), K_3PO_4 (1 eq.), DMSO (3 mL), air atmosphere, 395 nm lamp (36 W), 30–35 °C, 24 h.
[b] Conversion and selectivity were determined by GC-MS analysis using dodecane as an internal standard.

moderate to high conversion and selectivity. We also conducted a scale-up study by increasing the concentration of substrate **1a** by 10-fold compared to the standard reaction conditions used during optimization (as shown in Table 1). The resulting azo product (**2a**) was obtained with a selectivity of 96% and a conversion rate of 52% after 24 hours. Extending the reaction time to 48 hours increased the conversion to 82% while maintaining consistent selectivity, underscoring the practical applicability of our approach (refer to Fig. S3).

A review of previously documented catalysts for the formation of azo bonds reveals that several metal-based catalysts provide efficient conversion, but require a high amount of catalyst, the use of stoichiometric reagents, and strong oxidizing agents (Table S2). Comparing these prior studies with our work allows us to evaluate the advancements in catalytic efficiency, reaction conditions, selectivity, and environmental sustainability. In a recent study, molybdenum-based catalysts were used for the thermal oxidative coupling of amines to produce azoaromatics. This process involved the use of H_2O_2 as the oxidant and $Na_2S_2O_3$ as an additive.[80] Qu and co-workers innovatively employed single-crystal MnOOH nanotubes to synthesize azo compounds from amines, demonstrating exceptional performance under thermal conditions, albeit requiring high-pressure oxygen (5 bar).[81] Another research endeavour explored the utilization of $Zr(OH)_4$ to oxidize anilines to azobenzenes, employing acetic acid as the solvent and TBHP as the oxidant.[82] Numerous other studies have reported the synthesis of azoaromatics using strong oxidants like TBHP and H_2O_2, under both thermal and photocatalytic setups, often employing metal-based catalysts.[44,46,47] Moreover, Vannucci and co-workers reported homogeneous Ir-based photocatalysts, showcasing their potential for azoaromatics synthesis from amines under aerial conditions; however, the notable drawbacks of high iridium loading (5 mol%) and limited substrate scope highlight certain constraints.[27]

In our investigation, we assessed the sustainability of our approach by examining factors such as metal cost, temperature, oxidant use, yield, substrate scope, and catalyst reusability, and compared these with the existing literature (Fig. 7g). Many reported catalysts often required high temperature, strong oxidants, and expensive noble or other transition metal-based catalysts, which may pose issues related to sustainability (Fig. 7g and Table S2). In contrast, mpg-C_3N_4 demonstrates strong photocatalytic activity in a fully metal-free environment, maintaining its performance even after five cycles. Our method emphasizes greener, low-cost, and more sustainable practices, delivering high efficiency and selectivity across various substrates, showcasing the advantages of photocatalysis over traditional metal-dependent systems.

2.3 Mechanistic studies

In order to investigate the reaction mechanism, a series of comparative experiments was conducted. Under ideal reaction conditions, air was chosen as the oxidant for the photo-induced oxidative coupling of amines to produce azoaromatics, highlighting the environmentally friendly nature of this reaction system. This suggests that the pathway involving oxygen is predominant, indicating that a reactive oxidative species (ROS) is generated from O_2. To identify the specific type of ROS produced in this photocatalytic system, various radical scavengers were introduced to inhibit the production of singlet oxygen ($^1O_2$), hydroxyl radicals ($^{\bullet}OH$), and superoxide anion radicals ($O_2^{\bullet-}$), with the results shown in Fig. 5a. The introduction of *p*-benzoquinone (*p*-BQ), a known scavenger for $O_2^{\bullet-}$, resulted in no conversion, underscoring the essential role of photogenerated $O_2^{\bullet-}$ as a ROS in the reaction. Conversely, the addition of isopropanol (IPA), a scavenger for $^{\bullet}OH$, and sodium azide (NaN_3), a scavenger for $^1O_2$, did not significantly affect the reaction conversion, suggesting that $^{\bullet}OH$ and $^1O_2$ are not involved.[83,84] Furthermore, conducting the reaction with 2,2,6,6-tetramethyl-1-piperidinyloxyl (TEMPO) led to a substantial decrease in conversion, providing strong evidence that the reaction follows an amine radical pathway.[84] To support this hypothesis, a radical scavenging study was conducted using 2,6-di-*tert*-butyl-4-methylphenol (BHT) to capture the amine radical.[56] After 24 hours of irradiation, the reaction mixture was analyzed by HR-MS and GC-MS, revealing a distinct HR-MS peak for the *p*-anisidine–BHT adduct with a molecular weight of 342.2416 g mol^{-1} (Fig. S5). No product was formed in the presence of BHT, which confirmed the involvement of amine radicals in the reaction. Additionally, the use of potassium persulfate ($K_2S_2O_8$) as an electron scavenger[56] or triethylamine (TEA) as a hole scavenger[85] nearly halted the reaction, reinforcing the critical role of the photogenerated electron–hole pair in the photo redox process (Fig. 5a). Moreover, the generation of H_2O_2 as a byproduct from the superoxide radical was confirmed by adding a starch KI solution to the reaction mixture after photoreaction, which resulted in a dark blue-black colour (Fig. S6).[86,87] In addition, quantitative analysis using $KMnO_4$ redox titration[88] confirmed that approximately 20 μmol of H_2O_2 was generated as a byproduct under the standard reaction conditions.

The formation of $O_2^{\bullet-}$ was convincingly validated using EPR spectroscopy, with 5,5-dimethyl-1-pyrroline *N*-oxide (DMPO) as a spin-trap under standard reaction conditions. Under conditions devoid of light, no free radical response was detected *via* EPR, underscoring the necessity of light for this reaction. However, upon introducing DMPO to the reaction mixture and irradiating it with 395 nm light for 5 min, a distinct pattern of four well-defined peaks corresponding to DMPO–$O_2^{\bullet-}$ was observed (see Fig. 5b). The same pattern for the EPR spectra of mpg-C_3N_4 was observed under both dark and light irradiation conditions (Fig. S7). This result aligns well with previous studies, confirming that superoxide radical anions are the primary reactive species involved in the photocatalytic oxidative coupling of amines using mpg-C_3N_4.[21,89] Additionally, to determine the possible involvement of oxygen-containing intermediates, such as nitroso or nitro compounds in the reaction pathway, control experiments were conducted under standard conditions, and the results of these experiments suggest that oxygenated intermediates are unlikely to be involved in the reaction mechanism (Fig. S4).

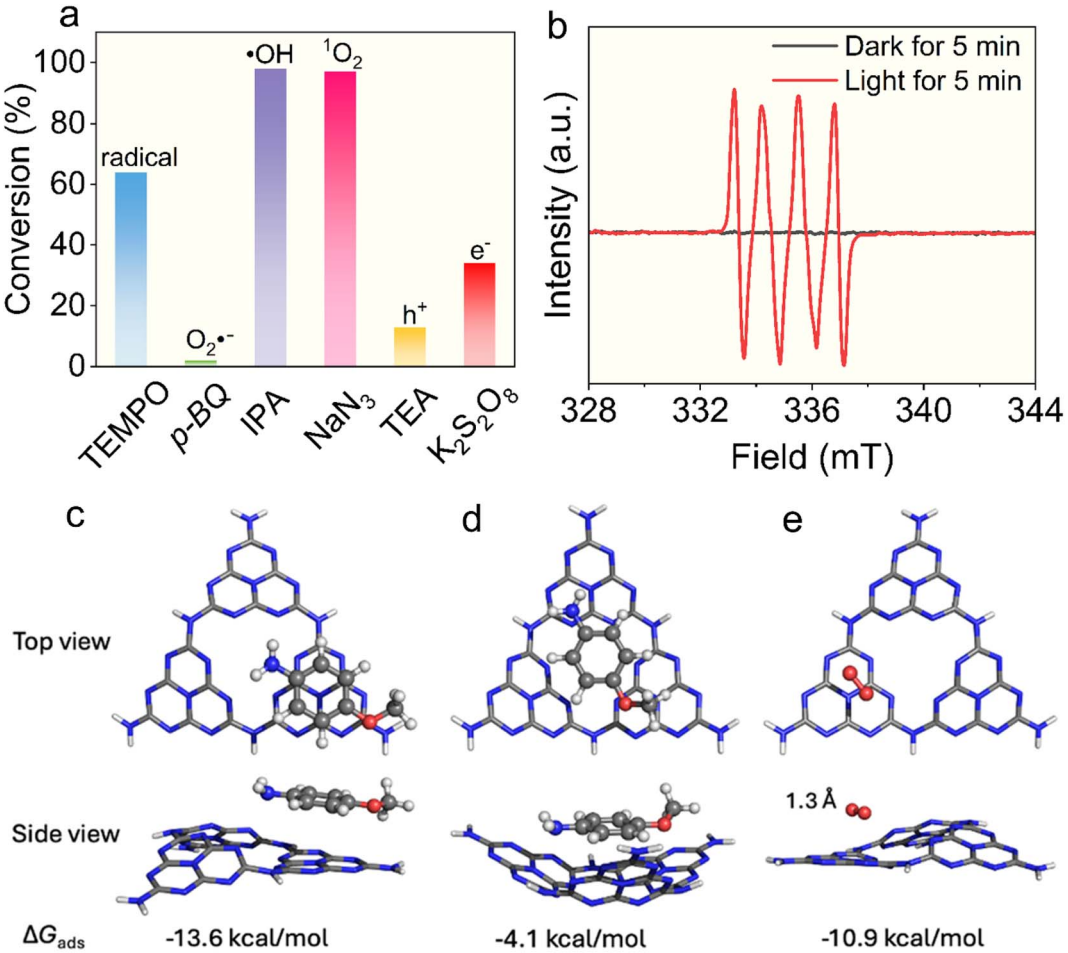

Fig. 5 (a) Scavenger study and (b) EPR spectrum of the DMPO–superoxide radical. Theoretical calculations for the adsorption of *p*-anisidine and the activation of O_2 on the mpg-C_3N_4 photocatalyst associated with the corresponding adsorption Gibbs energies (ΔG_{ads}): (c) *p*-anisidine on mpg-C_3N_4 (site 1), (d) *p*-anisidine on mpg-C_3N_4 (site 2), and (e) superoxide radical on mpg-C_3N_4. The O–O bond lengths in Å show the activation of O_2 and the formation of superoxide radicals. Nitrogen is shown in blue, carbon in grey, oxygen in red, and hydrogen in white.

The photocatalytic performance extends beyond the sensitive optical response and the generation of stable electron–hole pairs. Alongside the photogenerated charge carriers described earlier, the nature of the surface-active sites is crucial in driving the oxidative coupling of amines. Notably, FT-IR spectroscopy, XPS, BET, and CO_2-TPD analyses reveal that mpg-C_3N_4 features abundant nitrogen-rich functional motifs including –NH_x groups, bridging C–N–C linkages, and electron-rich sp^2 nitrogen species within the heptazine/triazine framework. These sites are known to facilitate substrate adsorption, activate amines, and stabilize nitrogen-centered radical intermediates.[90–92] Furthermore, the mesoporous architecture and high surface area of mpg-C_3N_4 promote the accessibility of these active centers, leading to strengthened interactions among the catalyst surface, amines, and reactive oxygen species.[93] These structural features collectively play a significant role in enhancing the photocatalytic efficiency.

Crucially, it is also essential to consider how reactive molecules, such as the substrate and O_2, interact with the true active sites of the mpg-C_3N_4 photocatalyst. To this end, DFT calculations were performed to investigate the function of mpg-C_3N_4 in the photocatalytic aerobic oxidative coupling of aryl amines to afford azoaromatics, with particular focus on the activation of oxygen species. Guided by XPS characterization, a tri-*s*-triazine structural model of mpg-C_3N_4 was utilized for the simulations. The adsorption studies of *p*-anisidine on the catalyst revealed an adsorption Gibbs energy of −13.6 kcal mol^{-1}. Notably, *p*-anisidine displayed π–π stacking interactions atop the tri-*s*-triazine unit (Fig. 5c), demonstrating a preference for this orientation over adsorption within the mesoporous cavities of mpg-C_3N_4. In the latter case, a more pronounced distortion of the mpg-C_3N_4 model was observed, reducing ΔG_{ads} to −4.1 kcal mol^{-1} (Fig. 5d). The dependence of adsorption strength on the adsorption site aligns with previous reports regarding the adsorption of benzyl alcohol on polymeric carbon nitride.[94] Consequently, the structural integrity of mpg-C_3N_4 facilitates the efficient interaction of aromatic amines with the catalyst surface, thereby enhancing its role as a support in oxidative coupling reactions.

Furthermore, aligning with the radical trap experiments, the adsorption of superoxide radical (Fig. 5e) was examined to understand the activation of reactive oxygen species. The

superoxide radical demonstrated an adsorption Gibbs energy of −10.9 kcal mol^{-1}, and the optimized model of O_2@mpg-C_3N_4 revealed an elongated O–O bond length of 1.3 Å in contrast to the 1.2 Å bond length of molecular O_2, which was also observed for the Mn_1/tri-CN photocatalyst.[91] A Wiberg bond index (WBI) analysis indicated a bond order of 1.3, confirming the formation of the superoxide radical and implicating its key role in the oxidative coupling of aryl amines to generate azoaromatics. These findings underscore the critical role of mpg-C_3N_4 not only as a structural support but also as an active platform that facilitates and enhances the adsorption and activation of reactants in oxidative coupling reactions.

Taking into account the above-mentioned experimental and theoretical results, along with the previously reported reaction mechanism, we investigated the reaction pathway for the light-driven oxidative coupling of amines.[27,95] Upon light irradiation, mpg-C_3N_4 generates electron–hole pairs; the photogenerated electrons reduce O_2 to superoxide radicals ($O_2^{\bullet-}$), while the holes oxidize the amines to their corresponding radical cations.[56] As illustrated in Fig. 6, the transformation of *p*-anisidine into azo compounds proceeds through a sequence of radical formation, proton transfer, homocoupling, and stepwise oxidation processes. After the adsorption of a reactant onto mpg-C_3N_4 with a Gibbs energy of −14 kcal mol^{-1}, the reaction begins with the hole transfer and formation of superoxide radicals (Fig. 6, step a), a step that is thermodynamically feasible under direct light at a temperature of 313 K, with a reaction Gibbs energy of 22 kcal mol^{-1}. This is followed by a key activation step where a superoxide radical ($O_2^{\bullet-}$) oxidizes the aniline to a nitrogen-centered radical, showing a reaction Gibbs energy of 9 kcal mol^{-1} (Fig. 6, step b). The pivotal event in the sequence is the homocoupling of two nitrogen-centered

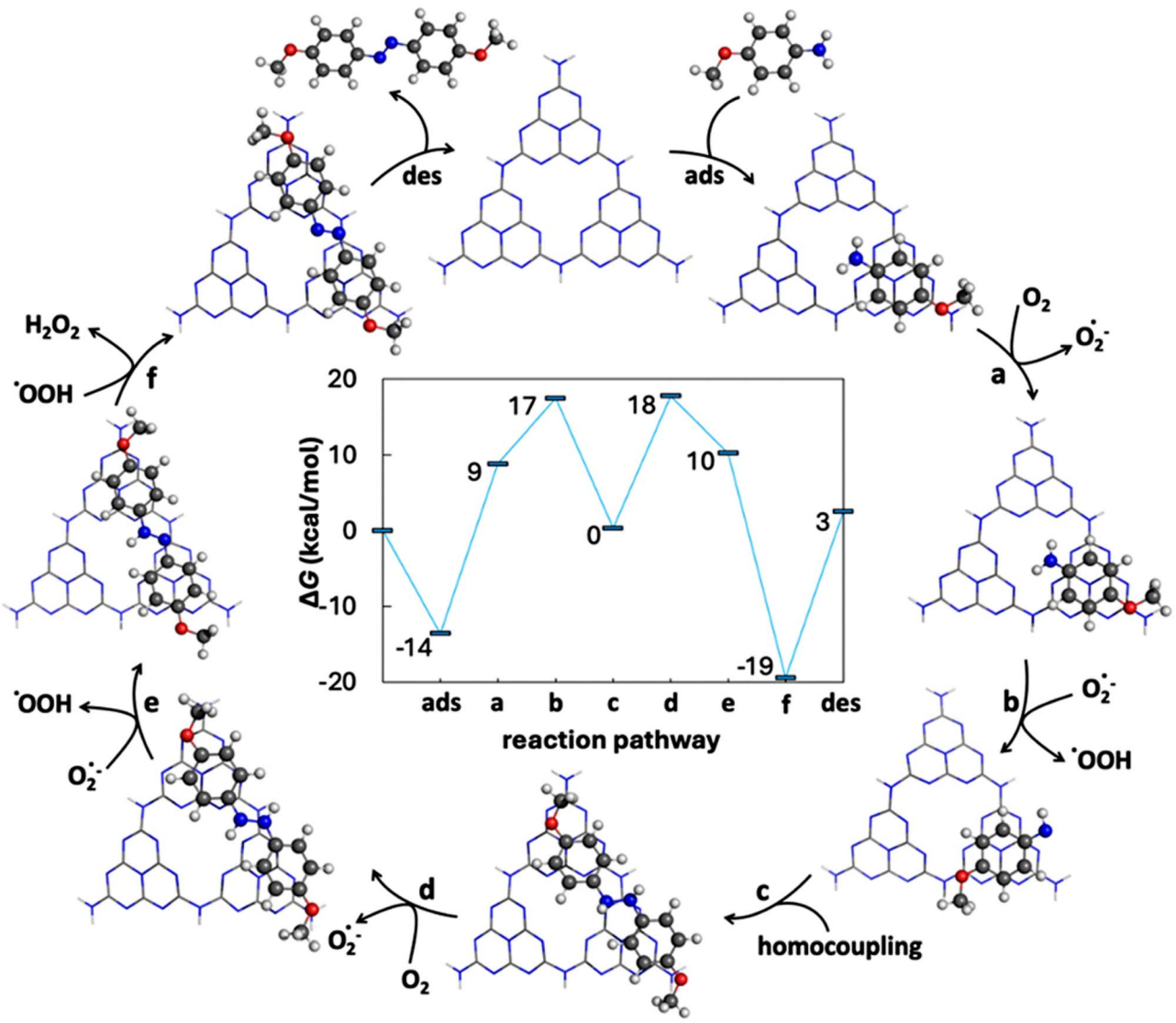

Fig. 6 (a–f) Proposed reaction mechanism and reaction profile of the photocatalytic aerobic oxidative coupling of aryl amines catalyzed by mpg-C_3N_4. The model of the mpg-C_3N_4 photocatalyst is shown in sticks. The geometries of reactants, reaction intermediates, and products adsorbed on the catalyst surface are shown in ball-and-stick models. Carbon is shown in gray, oxygen in red, hydrogen in white, and nitrogen in blue.

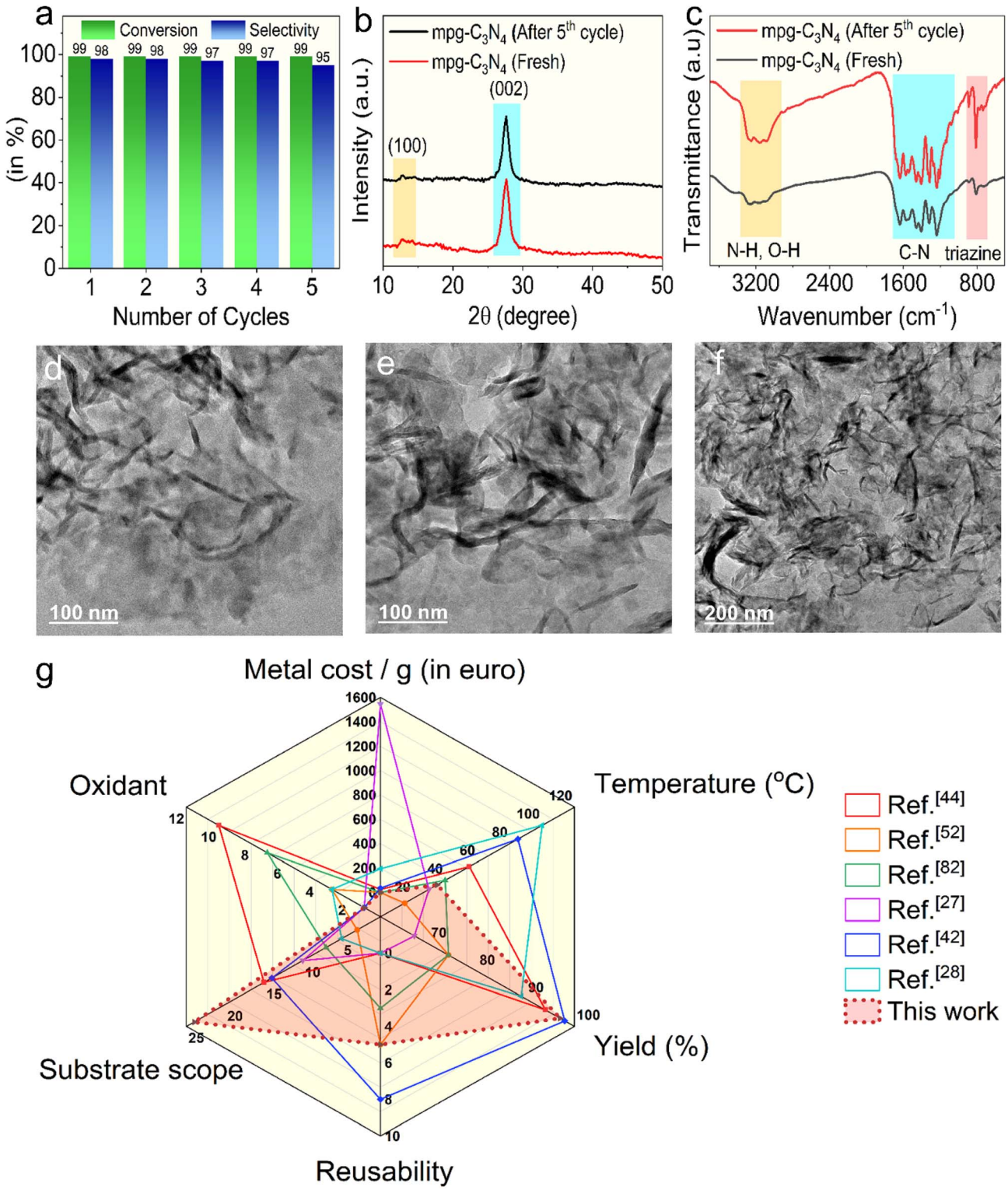

Fig. 7 (a) Recyclability study. (b) XRD patterns of the fresh and reused (after the 5th cycle) mpg-C_3N_4. (c) FT-IR spectra of the fresh and reused (after the 5th cycle) mpg-C_3N_4. HR-TEM images of (d) fresh mpg-C_3N_4 and (e and f) reused (after the 5th cycle) mpg-C_3N_4. (g) Sustainability assessment comparison of the mpg-C_3N_4 photocatalyst with other photocatalysts reported in the literature in terms of metal cost (calculated based on the price of metal salts used in the study or for the preparation of the catalyst from Sigma-Aldrich), temperature, yield, reusability, substrate scope, and oxidant used (a scale of 1–10 indicates the oxidizing capability: 1 = air, 3 = O_2, 5 = H_2O_2, 7 = TBHP, and 10 = O_2 + H_2O_2).

radicals (Fig. 6, step c), which forges the N–N bond, with a reaction Gibbs energy of −17 kcal mol^{-1}. Subsequent oxidative steps mediated by ROS, such as superoxide and hydroperoxyl radicals (HOO$^{\bullet}$), convert the hydrazine intermediate to azoaromatics, with each step proceeding through energetically favorable or accessible pathways (Fig. 6, steps d–f).

These findings indicate that the catalytic role of mpg-C_3N_4 is related to the generation of superoxide radicals as well as the special organization of reactants on the catalyst surface (Fig. 6).

2.4 Stability studies

Sustainability and reusability are critical factors in assessing high-performance catalysts, particularly photocatalysts, where the effectiveness is closely related to their ability to be reused. To evaluate the reusability and stability of mpg-C_3N_4 photocatalysts, the catalyst was extracted from the reaction medium using centrifugation and thoroughly washed several times with DMSO, H_2O, and EtOH. Recycling tests were conducted over five consecutive cycles under standard reaction conditions. As shown in Fig. 7a, mpg-C_3N_4 retained its catalytic efficiency with no significant decline after five cycles. Furthermore, the structural and morphological integrity of the recycled catalyst was examined through a range of characterization techniques such as XRD, FT-IR spectroscopy, and HR-TEM analysis. The XRD and FT-IR spectra of the recycled mpg-C_3N_4 sample after five cycles closely resembled those of the freshly synthesized mpg-C_3N_4 sample, demonstrating the remarkable stability of this heterogeneous photocatalyst (Fig. 7b and c). A slight enhancement in the FT-IR absorption intensity of the triazine (800 cm^{-1}) and N–H/O–H (~3000 cm^{-1}) bands was observed for the reused catalyst after the 5th cycle, which could be due to minor structural modifications or the surface-adsorbed species that accumulate during repeated use (Fig. 7c). Furthermore, HR-TEM analysis confirmed that the nanowire morphology of mpg-C_3N_4 was preserved even after five cycles (Fig. 7d–f). In summary, the robust and reusable characteristics of mpg-C_3N_4 photocatalysts ensure reliable performance under standard reaction conditions, underscoring their potential for sustainable catalytic applications.

3 Conclusions

In summary, we have successfully developed a metal-free mpg-C_3N_4 photocatalyst using a straightforward one-step thermal polymerization method and utilized it for the photocatalytic oxidative coupling of arylamines to generate aromatic azo compounds under mild conditions. This metal-free mpg-C_3N_4 photocatalyst exhibited exceptional activity across a diverse range of substrates, including both electron-rich and electron-deficient amines, achieving conversions and selectivities up to 99%. The ability of the mpg-C_3N_4 photocatalyst to harness light, combined with its high surface area, mesoporous structure, and efficient charge transfer and separation, significantly enhances its photocatalytic performance. The mechanism underlying the photocatalytic oxidative coupling of amines has been explored through a series of control experiments, EPR spectroscopy, and DFT studies. These mechanistic investigations revealed that the mpg-C_3N_4 photocatalyst can activate atmospheric O_2 molecules to produce superoxide radical anions ($O_2^{\bullet-}$), which are highly reactive species. Importantly, this photocatalyst retained its catalytic efficiency over five cycles without any significant loss. The mild and environmentally friendly reaction conditions utilizing light as the irradiation source, an aerial atmosphere, and a metal-free photocatalyst render the mpg-C_3N_4-catalyzed process both green and sustainable. As the demand for eco-friendly approaches in chemical synthesis surges, our findings not only lay the foundation for ground-breaking advancement in photocatalyst design and application but also contribute significantly to the global quest for sustainable methods that reduce environmental impacts and enhance resource efficiency. In the future, this mpg-C_3N_4 catalyst may also be explored for other photocatalytic transformations, including oxidative or reductive functionalization, C–N/C–C bond-forming reactions, and the upgrading of biomass-derived substrates.

Author contributions

Dinesh S. Chaudhari: writing – review & editing, writing – original draft, methodology, investigation, formal analysis, conceptualization. Rahul P. Gaikwad: writing – review & editing, formal analysis. Indrajeet R. Warkad: writing – review & editing, formal analysis. Rostislav Langer and Michal Otyepka: theoretical calculations, writing – DFT section. Manoj B. Gawande: writing – review & editing, visualization, validation, supervision, project administration, methodology, investigation, funding acquisition, formal analysis, data curation, conceptualization.

Conflicts of interest

The authors confirm that there are no financial conflicts of interest or personal relationships that could have impacted the work described in this paper.

Data availability

The data supporting this article are provided within the supplementary information (SI). Supplementary information is available. See DOI: https://doi.org/10.1039/d5ta08970k.

Acknowledgements

D. S. C. and I. R. W. express their gratitude to the Institute of Chemical Technology (ICT), Mumbai-Marathwada Campus, Jalna, for providing the facilities for doctoral studies. R. P. G. acknowledges the Council of Scientific and Industrial Research (CSIR), New Delhi, for granting the research fellowship for his doctoral research. D. S. C. and M. B. G. acknowledge the financial support from the DST-SERB Core Research Grant (CRG/2021/001738). This work was supported by the Ministry of Education, Youth and Sports of the Czech Republic through the e-INFRA CZ (ID: 90254). M. O. acknowledges the support of MEYS through the ERDF/ESF project TECHSCALE (No. CZ.02.01.01/00/22_008/0004587). M. O. also acknowledges the financial support from the European Union through the REFRESH project – Research Excellence For REgion Sustainability and High-tech Industries (CZ.10.03.01/00/22_003/0000048), funded *via* the Operational Programme Just Transition.

References

1 J. Huo and C. Peng, *Resour. Policy*, 2023, **86**, 104049.
2 J. Wang and W. Azam, *Geosci. Front.*, 2024, **15**, 101757.
3 W.-J. Ong, L.-L. Tan, Y. H. Ng, S.-T. Yong and S.-P. Chai, *Chem. Rev.*, 2016, **116**, 7159–7329.
4 B. Ran, L. Ran, Z. Wang, J. Liao, D. Li, K. Chen, W. Cai, J. Hou and X. Peng, *Chem. Rev.*, 2023, **123**, 12371–12430.
5 L. Buglioni, F. Raymenants, A. Slattery, S. D. A. Zondag and T. Noël, *Chem. Rev.*, 2022, **122**, 2752–2906.
6 A. Galushchinskiy, R. González-Gómez, K. McCarthy, P. Farràs and A. Savateev, *Energy Fuels*, 2022, **36**, 4625–4639.
7 P. Sharma, S. Kumar, O. Tomanec, M. Petr, J. Z. Chen, J. T. Miller, R. S. Varma, M. B. Gawande and R. Zbořil, *Small*, 2021, **17**, 2006478.
8 R. P. Gaikwad, I. R. Warkad, D. S. Chaudhari, S. Jiang, J. T. Miller, H. N. Pham, A. Datye and M. B. Gawande, *J. Colloid Interface Sci.*, 2024, **676**, 485–495.
9 P. Li, J. A. Terrett and J. R. Zbieg, *ACS Med. Chem. Lett.*, 2020, **11**, 2120–2130.
10 T. T. Salunkhe, T. R. Gurugubelli, B. Viswanadham, B. Babu, T. V. M. Sreekanth and K. Yoo, *J. Chem.*, 2025, **2025**, 8849437.
11 B. Singh, V. Sharma, R. P. Gaikwad, P. Fornasiero, R. Zbořil and M. B. Gawande, *Small*, 2021, **17**, 2006473.
12 R. Paul, I. R. Warkad, S. Arulkumar, S. Parthiban, H. R. Darji, M. Naushad, R. G. Kadam and M. B. Gawande, *Mol. Catal.*, 2022, **530**, 112566.
13 R. P. Gaikwad, D. R. Naikwadi, A. V. Biradar and M. B. Gawande, *ACS Appl. Nano Mater.*, 2023, **6**, 1859–1869.
14 X. Li, Q. Cheng, Y. Zhang, Y. Liu, Y. Pan, D. Zhao, S. Xiong, W. Liu, X. Jiang, J. Yan, X. Duan, Y. Tian and X. Li, *Angew. Chem., Int. Ed.*, 2025, **64**, e202424435.
15 C. Karthikeyan, P. Arunachalam, K. Ramachandran, A. M. Al-Mayouf and S. Karuppuchamy, *J. Alloys Compd.*, 2020, **828**, 154281.
16 J. Wang and S. Wang, *Coord. Chem. Rev.*, 2022, **453**, 214338.
17 G. F. S. R. Rocha, M. A. R. da Silva, A. Rogolino, G. A. A. Diab, L. F. G. Noleto, M. Antonietti and I. F. Teixeira, *Chem. Soc. Rev.*, 2023, **52**, 4878–4932.
18 S. Das, K. Murugesan, G. J. V. Rodríguez, J. Kaur, J. P. Barham, A. Savateev, M. Antonietti and B. König, *ACS Catal.*, 2021, **11**, 1593–1603.
19 A. Savateev, I. Ghosh, B. König and M. Antonietti, *Angew. Chem., Int. Ed.*, 2018, **57**, 15936–15947.
20 I. Ghosh, J. Khamrai, A. Savateev, N. Shlapakov, M. Antonietti and B. König, *Science*, 2019, **365**, 360–366.
21 J. Bai, S. Yan, Z. Zhang, Z. Guo and C.-Y. Zhou, *Org. Lett.*, 2021, **23**, 4843–4848.
22 X. Wang, K. Maeda, A. Thomas, K. Takanabe, G. Xin, J. M. Carlsson, K. Domen and M. Antonietti, *Nat. Mater.*, 2009, **8**, 76–80.
23 A. Kumar, P. Raizada, V. K. Thakur, V. Saini, A. A. P. Khan, N. Singh and P. Singh, *Chem. Eng. Sci.*, 2021, **230**, 116219.
24 L. Ma, Y. Gao, B. Wei, L. Huang, N. Zhang, Q. Weng, L. Zhang, S. F. Liu and R. Jiang, *ACS Catal.*, 2024, **14**, 2775–2786.
25 Y. Zhao, Z. Wang, X. Wang, P. Sun, F. Meng, G. Yang, X. Zhou, J. Wang, X. Zhang and G. Lyu, *Adv. Funct. Mater.*, 2025, **35**, 2422264.
26 K. S. Lakhi, D.-H. Park, K. Al-Bahily, W. Cha, B. Viswanathan, J.-H. Choy and A. Vinu, *Chem. Soc. Rev.*, 2017, **46**, 72–101.
27 J. D. Sitter and A. K. Vannucci, *J. Am. Chem. Soc.*, 2021, **143**, 2938–2943.
28 A. Grirrane, A. Corma and H. García, *Science*, 2008, **322**, 1661–1664.
29 S. Crespi, N. A. Simeth and B. König, *Nat. Rev. Chem.*, 2019, **3**, 133–146.
30 L. De Boni, E. Piovesan, L. Misoguti, S. C. Zílio and C. R. Mendonca, *J. Phys. Chem. A*, 2007, **111**, 6222–6224.
31 A. Bafana, S. S. Devi and T. Chakrabarti, *Environ. Rev.*, 2011, **19**, 350–371.
32 N. N. Riaz, S. Iqbal, S. Amin, K. Ahmad, M. Atif, S. Muhammad, M. M. Ahmed and M. Ashfaq, *J. Mol. Struct.*, 2025, **1321**, 139705.
33 C. Fedele, P. A. Netti and S. Cavalli, *Biomater. Sci.*, 2018, **6**, 990–995.
34 B. Zhang, Y. Feng and W. Feng, *Nano-Micro Lett.*, 2022, **14**, 138.
35 F. Cuétara-Guadarrama, M. Vonlanthen, K. Sorroza-Martínez, I. González-Méndez and E. Rivera, *Dyes Pigm.*, 2021, **194**, 109551.
36 E. Merino, *Chem. Soc. Rev.*, 2011, **40**, 3835–3853.
37 L. Wang, A. Ishida, Y. Hashidoko and M. Hashimoto, *Angew. Chem., Int. Ed.*, 2017, **56**, 870–873.
38 M. K. Sahoo, K. Saravanakumar, G. Jaiswal and E. Balaraman, *ACS Catal.*, 2018, **8**, 7727–7733.
39 H. Zhu, X. Ke, X. Yang, S. Sarina and H. Liu, *Angew. Chem., Int. Ed.*, 2010, **49**, 9657–9661.
40 C. Zhang and N. Jiao, *Angew. Chem., Int. Ed.*, 2010, **49**, 6174–6177.
41 S. Cai, H. Rong, X. Yu, X. Liu, D. Wang, W. He and Y. Li, *ACS Catal.*, 2013, **3**, 478–486.
42 A. Saha, S. Payra, B. Selvaratnam, S. Bhattacharya, S. Pal, R. T. Koodali and S. Banerjee, *ACS Sustainable Chem. Eng.*, 2018, **6**, 11345–11352.
43 M. Kumar, K. Soni, G. D. Yadav, S. Singh and S. Deka, *Appl. Catal., A*, 2016, **525**, 50–58.
44 H. Song, J. Wei, Z. Wang, Y. Liu, S. Zhao, X. Cai, Y. Xiao, L. Yang, P. Bai, L. Fang, F. Yang, S. Zheng, W. Zhang, J. Pan and C. Xu, *ACS Catal.*, 2024, **14**, 12372–12384.
45 X. Deng, X. Liu, S. Xia, H. Zhao, Y. Liu, Q. Ding and H. Zhang, *Colloids Surf., A*, 2023, **677**, 132352.
46 S. Agarwal, B. Dowara, S. Kumar, V. Kumar and K. Deori, *ACS Omega*, 2022, **7**, 48615–48622.
47 Q. Niu, Q. Huang, T.-Y. Yu, J. Liu, J.-W. Shi, L.-Z. Dong, S.-L. Li and Y.-Q. Lan, *J. Am. Chem. Soc.*, 2022, **144**, 18586–18594.
48 A. R. Patel, G. Patel, G. Maity, S. P. Patel, S. Bhattacharya, A. Putta and S. Banerjee, *ACS Omega*, 2020, **5**, 30416–30424.
49 S. Singh, V. Agarwal, T. K. Sarma and T. K. Mukherjee, *Green Chem.*, 2023, **25**, 9109–9114.
50 S. Singh and T. K. Mukherjee, *Chem. Sci.*, 2024, **15**, 13949–13957.

51 W. Chen, H. Li, Y. Jin, C. Wu, Z. Yuan, P. Ma, J. Wang and J. Niu, *Chem. Commun.*, 2022, **58**, 9902–9905.
52 X. Han, T. Zhang, X. Wang, Z. Zhang, Y. Li, Y. Qin, B. Wang, A. Han and J. Liu, *Nat. Commun.*, 2022, **13**, 2900.
53 C. Wang, B. Hu, X. Guo and L. Lei, *Green Chem.*, 2024, **26**, 6470–6479.
54 M. Fronczak, E. Tálas, Z. Pászti, G. P. Szijjártó, J. Mihály, A. Tompos, P. Baranowski, S. K. Tiwari and M. Bystrzejewski, *Diamond Relat. Mater.*, 2022, **125**, 109006.
55 L. Florentino-Madiedo, E. Díaz-Faes and C. Barriocanal, *Carbon*, 2022, **187**, 462–476.
56 A. Shi, K. Sun, Y. Wu, P. Xiang, I. B. Krylov, A. O. Terent'ev, X. Chen and B. Yu, *J. Catal.*, 2022, **415**, 28–36.
57 J. Lu, Z. Chen, Y. Shen, H. Yuan, X. Sun, J. Hou, F. Guo, C. Li and W. Shi, *J. Colloid Interface Sci.*, 2024, **670**, 428–438.
58 J. Xu, M. Fujitsuka, S. Kim, Z. Wang and T. Majima, *Appl. Catal., B*, 2019, **241**, 141–148.
59 Y. Gao, J. Duan, X. Zhai, F. Guan, X. Wang, J. Zhang and B. Hou, *J. Nanopart. Res.*, 2021, **23**, 44.
60 P. Xia, G. Li, X. Li, S. Yuan, K. Wang, D. Huang, Y. Ji, Y. Dong, X. Wu, L. Zhu, W. He and L. Qiao, *Crystals*, 2022, **12**, 1719.
61 D. Feng, Y. Cheng, J. He, L. Zheng, D. Shao, W. Wang, W. Wang, F. Lu, H. Dong, H. Liu, R. Zheng and H. Liu, *Carbon*, 2017, **125**, 454–463.
62 J. Liu, T. Zhang, Z. Wang, G. Dawson and W. Chen, *J. Mater. Chem.*, 2011, **21**, 14398–14401.
63 H. Chand, A. Kumar, S. Goswami and V. Krishnan, *Fuel*, 2024, **357**, 129757.
64 T. Wasiak and D. Janas, *J. Alloys Compd.*, 2022, **892**, 162158.
65 M. Li, L. Zhang, X. Fan, M. Wu, M. Wang, R. Cheng, L. Zhang, H. Yao and J. Shi, *Appl. Catal., B*, 2017, **201**, 629–635.
66 L.-y. Li, H. Gu, V. Šrot, P. van Aken and J. Bill, *J. Mater. Sci. Technol.*, 2019, **35**, 2851–2858.
67 S. Martha, A. Nashim and K. M. Parida, *J. Mater. Chem. A*, 2013, **1**, 7816–7824.
68 J. Oh, J. M. Lee, Y. Yoo, J. Kim, S.-J. Hwang and S. Park, *Appl. Catal., B*, 2017, **218**, 349–358.
69 J.-P. Zou, L.-C. Wang, J. Luo, Y.-C. Nie, Q.-J. Xing, X.-B. Luo, H.-M. Du, S.-L. Luo and S. L. Suib, *Appl. Catal., B*, 2016, **193**, 103–109.
70 C. Cheng, J. Shi, L. Wen, C.-L. Dong, Y.-C. Huang, Y. Zhang, S. Zong, Z. Diao, S. Shen and L. Guo, *Carbon*, 2021, **181**, 193–203.
71 S. Yang, Y. Gong, J. Zhang, L. Zhan, L. Ma, Z. Fang, R. Vajtai, X. Wang and P. M. Ajayan, *Adv. Mater.*, 2013, **25**, 2452–2456.
72 J. Liu, J. Yan, H. Ji, Y. Xu, L. Huang, Y. Li, Y. Song, Q. Zhang, H. Xu and H. Li, *Mater. Sci. Semicond. Process.*, 2016, **46**, 59–68.
73 J. Chen, C. Shen, B. Guo, Y. Yu and L. Wu, *Catal. Today*, 2019, **335**, 312–318.
74 M. Devi, M. H. Barbhuiya, B. Das, B. Bhuyan and S. S. Dhar, *Sustain. Energy Fuels*, 2020, **4**, 3537–3545.
75 M. Shen, L. Zhang, M. Wang, J. Tian, X. Jin, L. Guo, L. Wang and J. Shi, *J. Mater. Chem. A*, 2019, **7**, 1556–1563.
76 Y. Zhang, J. Liu, G. Wu and W. Chen, *Nanoscale*, 2012, **4**, 5300–5303.
77 M. A. Quintana, R. R. Solís, G. Blázquez, M. Calero and M. J. Muñoz-Batista, *Appl. Surf. Sci.*, 2024, **656**, 159717.
78 Y. Yang, G. Zeng, D. Huang, C. Zhang, D. He, C. Zhou, W. Wang, W. Xiong, B. Song, H. Yi, S. Ye and X. Ren, *Small*, 2020, **16**, 2001634.
79 R. P. Gaikwad, I. R. Warkad, D. S. Chaudhari, H. N. Pham, A. K. Datye and M. B. Gawande, *J. Colloid Interface Sci.*, 2025, **679**, 54–63.
80 S. Han, Y. Cheng, S. Liu, C. Tao, A. Wang, W. Wei, H. Yu and Y. Wei, *Angew. Chem., Int. Ed.*, 2021, **60**, 6382–6385.
81 Y. Zou, M. Zhang, F. Cao, J. Li, S. Zhang and Y. Qu, *J. Mater. Chem. A*, 2021, **9**, 19692–19697.
82 J. Qin, Y. Long, F. Sun, P.-P. Zhou, W. D. Wang, N. Luo and J. Ma, *Angew. Chem., Int. Ed.*, 2022, **61**, e202112907.
83 W. Zou, X.-H. Liu, C. Xue, X.-T. Zhou, H.-Y. Yu, P. Fan and H.-B. Ji, *Appl. Catal., B*, 2021, **285**, 119863.
84 G. Sportelli, G. Grando, M. Bevilacqua, G. Filippini, M. Melchionna and P. Fornasiero, *Chem.–Eur. J.*, 2023, **29**, e202301718.
85 A. Augustin, P. Ganguly, S. Shenoy, C. Chuaicham, S. C. Pillai, K. Sasaki, A. F. Lee and K. Sekar, *Adv. Sustain. Syst.*, 2024, **8**, 2400321.
86 L. Huang, J. Zhao, S. Guo, C. Zhang and J. Ma, *J. Org. Chem.*, 2013, **78**, 5627–5637.
87 M. K. Sahoo, G. Jaiswal, J. Rana and E. Balaraman, *Chem.–Eur. J.*, 2017, **23**, 14167–14172.
88 Y. Shiraishi, S. Kanazawa, Y. Sugano, D. Tsukamoto, H. Sakamoto, S. Ichikawa and T. Hirai, *ACS Catal.*, 2014, **4**, 774–780.
89 Y. Zhao and M. Antonietti, *Angew. Chem., Int. Ed.*, 2017, **56**, 9336–9340.
90 G. Grando, G. Sportelli, G. Filippini, M. Melchionna and P. Fornasiero, *Nano Trends*, 2023, **4**, 100028.
91 Z. Zhang, W. Liu, Y. Zhang, J. Bai and J. Liu, *ACS Catal.*, 2021, **11**, 313–322.
92 M. Yang, R. Lian, X. Zhang, C. Wang, J. Cheng and X. Wang, *Nat. Commun.*, 2022, **13**, 4900.
93 C. Xing, G. Yu, T. Chen, S. Liu, Q. Sun, Q. Liu, Y. Hu, H. Liu and X. Li, *Appl. Catal., B*, 2021, **298**, 120534.
94 J. Ma, F. Zhang, Y. Tan, S. Wang, H. Chen, L. Zheng, H. Liu and R. Li, *ACS Appl. Mater. Interfaces*, 2022, **14**, 18383–18392.
95 L. Kaur, M. Kumar and V. Bhalla, *Green Chem.*, 2023, **25**, 5240–5246.

